Characterization and comparison of Yb^{3+}-doped $YA1O_3$ perovskite crystals (Yb:YAP) with Yb^{3+}-doped $Y_3Al_5O_{12}$ garnet crystals (Yb:YAG) for laser application

G. Boulon,[1,2,*] Y. Guyot,[1] H. Canibano,[1] S. Hraiech,[1] and A. Yoshikawa[1,2]

[1]*Physical Chemistry of Luminescent Materials, University of Lyon, University Claude Bernard/Lyon1, UMR 5620 CNRS, Bât. A. Kastler, 10 rue Ampère, 69622 Villeurbanne Cedex, France*

[2]*Institute of Multidisciplinary Research for Advanced Materials, Tohoku University, 2-1-1 Katahira, Aoba-ku, Sendai 980-857, Japan*

[*]*Corresponding author: georges.boulon@pcml.univ-lyon1.fr*

Received November 26, 2007; revised February 19, 2008; accepted February 27, 2008; posted March 12, 2008 (Doc. ID 89887); published April 30, 2008

High-optical-quality single crystals of Yb^{3+}-doped $YAlO_3$ perovskite (Yb^{3+}:YAP) were grown by the Czochralski (CZ) method and characterized. From polarized absorption and emission spectra, assignment of the Yb^{3+} energy levels was proposed. Yb^{3+} concentration dependence of experimental decay times allows us to study concentration quenching and suggests both strong radiative and nonradiative energy transfers, from Yb^{3+} ions to impurities, well described by a limited diffusion model. Yb^{3+}:YAP crystal is a potentially useful polarized laser gain medium in laser-diode-pumped solid-state configurations. 5.7 at. % Yb^{3+} optimum concentration was deduced by prediction of laser performances. In addition, thermal properties and figure of merit, which is defined from our own model taking into account only spectroscopic data, were also compared with those of Yb^{3+}-doped YAG. © 2008 Optical Society of America

OCIS codes: 140.0140, 140.3580, 140.3615, 160.0160, 300.0300, 300.6250.

1. INTRODUCTION

Over the past decade, thanks to improvements of high-performance GaAs and InGaAs laser diodes with wavelengths between 900 and 1100 nm, interest in ytterbium doped crystals has been renewed for applications in high-efficiency (>50%) and high-power (>50 W/cm) diode-pumping laser systems. The trivalent ytterbium is the most promising ion that can be used in a non- Nd^{3+} laser in the same range. Its advantage over the Nd^{3+} ion is due to its very simple two-level energy scheme: the $^2F_{7/2}$ ground state and the $^2F_{5/2}$ excited state. There is no excited-state absorption reducing the effective laser cross section, and no upconversion, and no concentration quenching. The intense absorption lines are well suited for laser diode pumping near 980 nm, and the small Stokes shift between absorption and emission reduces the thermal loading of the material during laser operation. The disadvantage of Yb^{3+} is that the final laser level is thermally populated (quasi-three-level laser), increasing the threshold.

Our research program was prolonged to include this study on Yb^{3+}-doped solid-state laser crystals. Oxides have already been studied as YAG [1,2], GGG [3,4], LuAG [5], sesquioxides [6] in addition to fluorides as CaF_2 [7], $LiYF_4$ and $LiLuF_4$ [8], and KY_3F_{10}, recently published in this Journal [9]. Next we wish to publish results on another oxide called yttrium aluminate $YAlO_3$ (YAP).

YAP with a perovskite-type structure is a host for Nd^{3+}-doped solid-state lasers [10], Ce^{3+}-doped scintillators [11–13], and neutrino detection in high-energy physics [14]. Although YAP is a biaxial crystal with an orthorhombic space group, it has slightly weaker mechanical properties than $Y_3Al_5O_{12}$ (YAG) cubic crystals [15]. Compared with YAG, single crystals of YAP could be grown faster at a lower temperature (1850 °C instead of 1950 °C), with smaller cores and more favorable distribution coefficients for rare-earth dopants [16]. Very recently, charge transfer (CT) luminescence of Yb^{3+} ions in YAP was studied, and it showed well-shaped CT luminescence in the ultraviolet region peaking at 350 nm [17,18]. The very fast decay time in Yb^{3+}:YAP can be tuned in the temperature range of 80 to 300 K within two orders of magnitude (1–100 ns) at least, which could be an advantage in depth-of-interaction monitoring in positron emission tomography (PET) machines [19].

Indeed, our main approach is to publish undissociated results on both (1) crystal growth of high-quality single crystals, characterizations of spectroscopic and thermal properties, and position of the Yb^{3+}:YAP in the figure-of-merit we have previously defined, and then (2) the optimization of the gain from the laser model we have introduced—especially from concentration quenching analysis. Special efforts will also be made on the comparison with the Yb^{3+}:YAG reference.

 © 2008 Optical Society of America

2. GROWTH, COMPOSITION ANALYSIS, AND STRUCTURAL CHARACTERIZATION

A. Experimental Procedure

Y_2O_3, Al_2O_3, and Yb_2O_3 powders of 4N purity were used as starting materials without preliminary sintering. The starting melt compositions of $Y_{1-x}Yb_xAlO_3$ were varied as x=0.005, 0.02, 0.1, 0.2, 0.3, and 0.45. The Yb^{3+}-doped YAP single crystals were grown by the Czochralski method (CZ) with automatic diameter control and a radio frequency induction heating system using an iridium crucible (inner diameter 40 mm, depth 40 mm), except the $Y_{0.995}Yb_{0.005}AlO_3$, which was grown by the micro-pulling-down (μ-PD) method [20]. During CZ growth, pure dry argon atmosphere was used both for premelting the raw materials and for crystal growth. The crystals were grown on the oriented seeds in the ⟨100⟩ direction at a growth rate of 0.1 mm/h and a rotation rate of 12–13 rpm. After growth, the crystals were cooled at a rate of 60 K/h.

The x-ray diffraction (XRD) patterns of Yb^{3+}:YAP powders were obtained using a Rigaku RINT-V diffractometer with Cu K_a radiation (40 kV, 40 mA). The scan time and the step size were 2°/min and 0.02°, respectively. The 2θ angle examined was 10°–80°.

Quantitative analysis of the Yb^{3+} ion content along the pulled crystal was performed by electron probe microanalysis (EPMA). The density of Yb^{3+}:YAP $(Y_{1-x}Yb_x)AlO_3$ single crystals increased with the increase of the Yb^{3+} concentration. As for the density, from $YAlO_3$ (YAP)=5.498 g/cm^3 and $YbAlO_3$ (YbAP)=8.243 g/cm^3, the dependence of Yb^{3+} concentration is calculated as 5.52 g/cm^3 for x=0.02 to 6.733 g/cm^3 for x=0.45 doped one, and the difference between 0.02% and 45% is (6.733–5.498)/5.498=0.225 (22.5%).

B. Composition Analysis

The $Y_{1-x}Yb_xAlO_3$ crystals (with x=0.3) were transparent, crack free, and did not contain any visible defects or inclusions. As an example, a photo of the grown $Y_{0.98}Yb_{0.02}AlO_3$ single crystal is shown in Figure 1. The colorless crystal was transparent with a smooth, flat surface and the diameter was almost constant (~20 mm). To investigate the composition homogeneity of the grown crystals, Yb^{3+} and Y^{3+} distributions along the crystals were analyzed using the EPMA method, and the values of the effective segregation coefficients (k_{eff}) for the Yb^{3+} ion were calculated to be close to the unity like in the reference [21]:

$$C_s/C_0 = k_{eff}(1-g)^{k_{-1}\ eff}.$$

C_0 and C_s represent ion concentration in the starting melt and in the crystal at the solidification fraction (g), respectively. As an example, in 0.1%Yb^{3+}:YAP, $k_{eff}(Yb^{3+})$ =0.965 and $k_{eff}(Y^{3+})$=1.078.

Figure 2 shows that Yb^{3+}:YAP single crystals present a good composition along the growth axis on which the measurements were carried out. It can be seen that the concentration of the Yb^{3+} and Y^{3+} is almost identical to the initial composition with an experimental error of ~10% in the melt.

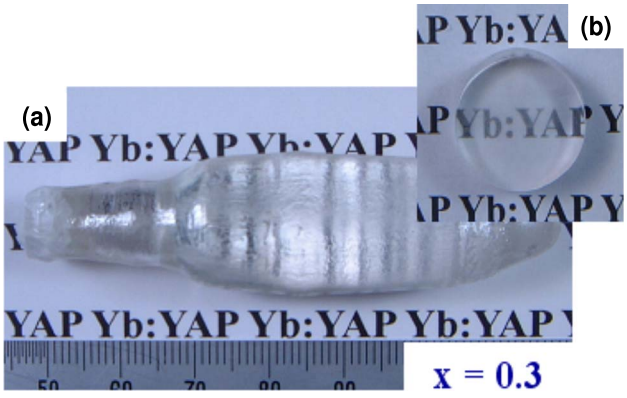

Fig. 1. (Color online) (a) Photo of Cz-grown $Y_{1-x}Yb_xAlO_3$ (with x=0.3) single crystal and (b) its cross section along the c axis.

C. Structural Characterization

Evolution of the powder x-ray diffraction as a function of the ytterbium concentration has already been reported [21,22]. A continuous solid solution was formed in the case of Yb^{3+}:YAP in the range of x=0.0 to 0.45. As the ytterbium concentration increased, the lattice constant along

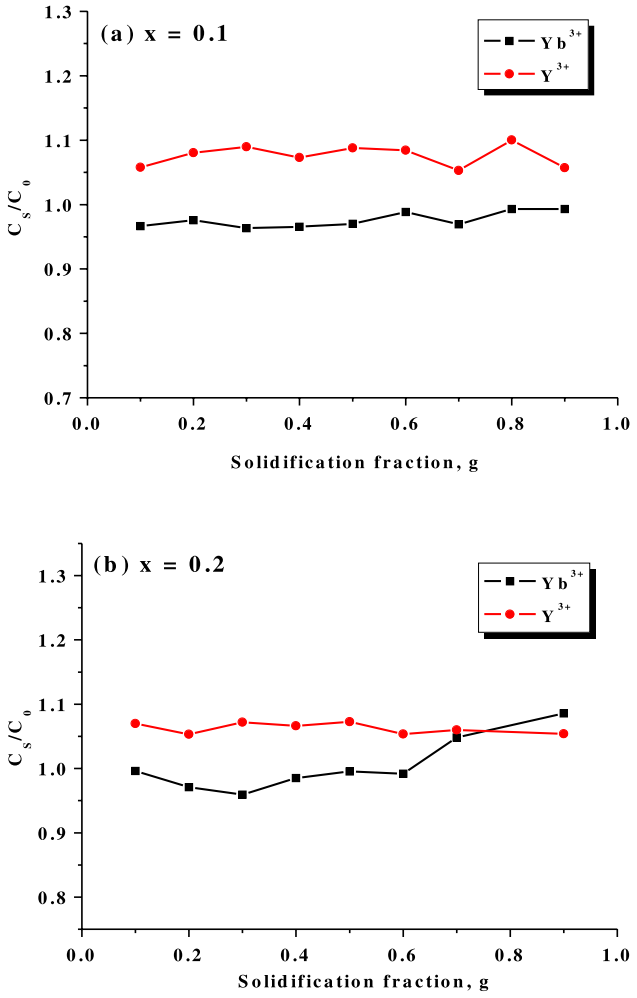

Fig. 2. (Color online) Variation of the chemical composition of $Y_{1-x}Yb_xAlO_3$ [with (a) x=0.1 and (b) x=0.2] single crystals observed on planes parallel to the growth axis. C_0 and C_s represent ion concentration in the starting melt and in the crystal at the solidification fraction (g), respectively.

the a and c axes decreased slightly, while along the b axis it increased to reach 5.3308 Å at 20% of Yb^{3+} and remained constant for higher Yb^{3+} concentrations (see Fig. 3). The unit-cell volume decreased, and the material density increased proportionally to the increase of Yb^{3+} concentration [21]. The crystal quality of the grown crystals was characterized by x-ray rocking curve measurements. ω scan was carried out for the reflection from the (004) plane corresponding to the ⟨001⟩ direction. The spectrum for $Y_{0.98}Yb_{0.02}AlO_3$ is shown in Fig. 4. It is shown that the full width at half maximum (FWHM) was measured to be around 57 arcsec. According to this result, we can suggest that Yb^{3+}:YAP single crystals, grown by the CZ method, show a good crystallinity and, naturally, Yb^{3+} can easily substitute Y^{3+} ions.

3. SPECTROSCOPIC PROPERTIES

A. Procedure of Spectroscopic Characterizations

Absorption spectra were measured with a Lambda 900 spectrophotometer equipped with a continuous flow helium refrigerator. Emission spectra were acquired by exciting the samples with a QUANTEL Nd^{3+}:YAG laser pumped dye laser using a mixture of the LD700 and DCM dyes. The dye laser light was converted to the 930–980 nm region by way of an H_2 Raman shift cell. The laser beam spot was about 500 μm in size, and the energy was about 0.8 mJ. The infrared emission was detected to be perpendicular to the excited beam with a Jobin–Yvon HRS1 monochromator equipped with a 1000 nm blazed grating, with a cooled Ge-detector, and the signal was processed with a STANFORD boxcar SRS 250. The visible emission was detected by an ORIEL spectrometer coupled with a gated intensified CCD camera (ANDOR/ORIEL INTASPEC V ICCD). The decay curves were recorded with a Lecroy LT 342 digital oscilloscope. The Raman spectrum was measured by a Dylor XY triple spectrometer using the 514.5 nm line of an ionized argon laser.

B. Absorption and Emission Spectra, Cross Sections, and Energy-Level Diagram

The room-temperature absorption and emission of polarized //a-axis spectrum $Y_{0.995}Yb_{0.005}AlO_3$ crystals are

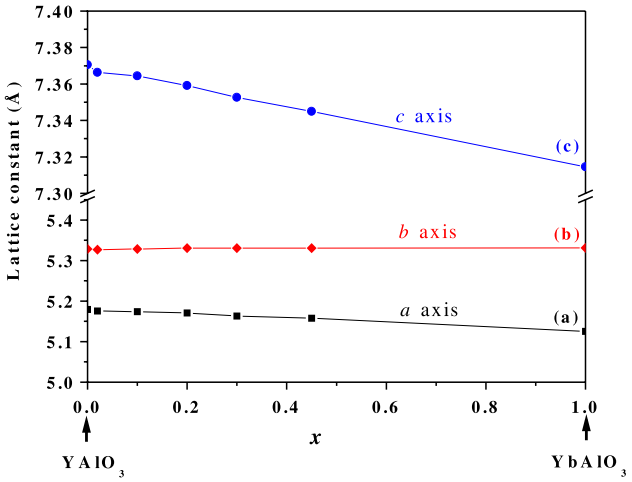

Fig. 3. (Color online) Yb^{3+} concentration dependence of the lattice constant along the a, b, and c axes of $Y_{1-x}Yb_xAlO_3$.

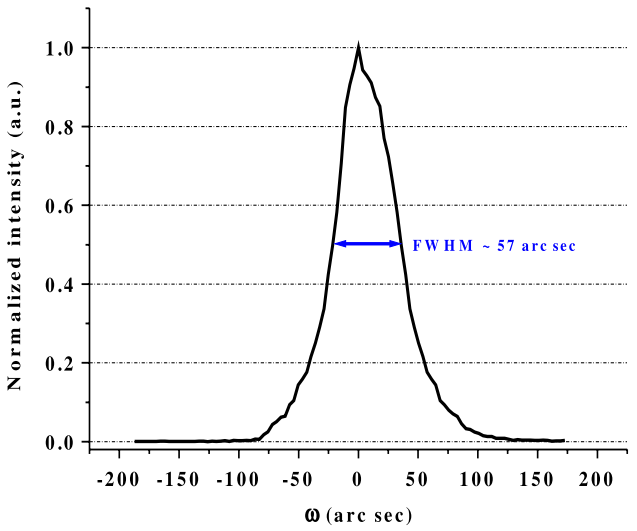

Fig. 4. (Color online) X-ray rocking curve of $Y_{1-x}Yb_xAlO_3$ (with x=0.1).

shown in Fig. 5. We chose one sample doped by the lowest (0.5 mol.%) concentration of Yb^{3+} ions to avoid cross-section calculation errors caused by a reabsorption effect mainly of resonant transitions. The emission cross-section value was calculated using the Füchtbauer–Ladenburg equation [23]. The $^2F_{7/2} \leftrightarrow {}^2F_{5/2}$ lowest energy resonant transition line was located at 980 nm. Other transitions between Stark levels were located from 920 nm to 1060 nm. The shapes of absorption and emission spectra are relatively broad for Yb^{3+} in substitution of the only Y^{3+} cation. The stimulated emission cross section at around 1010 nm was estimated to be 20×10^{-21} cm^2, which is a value identical to that of the highest intensity emission line of Yb^{3+}:YAG, which is, however, shifted at 1030 nm.

The assignment of Yb^{3+} Stark levels is known to have problems, since the appearance of a strong electron-phonon mixes both electronic and vibronic transitions of the main site. The electronic absorption transitions (1 $\rightarrow$5, 1$\rightarrow$6, 1$\rightarrow$7) and the resonant 5$\rightarrow$1 and non-resonant (5$\rightarrow$2, 5$\rightarrow$3, 5$\rightarrow$4) electronic emission transitions were observed as mentioned in the insert of Fig. 5. Additional vibronic lines can be also seen around 950 and 1030 nm. To identify electronic and vibronic peaks, our own experimental approach was also applied as with the previous crystals we have studied by comparing absorption, emission, and Raman spectra [1–9]. Finally, Stark level energies of the Yb^{3+} site in YAP are summarized in Table 1.

To verify our interpretation of Yb^{3+} energy levels, we applied the barycenter plot method, introduced by Antic–Fidancev [24], based on the fact that the spin orbit splitting between $^2F_{7/2}$ and $^2F_{5/2}$ is host independent and equal to the free-ion energy separation. For rare-earth ions, it was shown that the $^{2S+1}L_J$ level barycenter, as a function of any other barycenter of isolated levels in the $4f^n$ ground configuration, exhibits a linear dependence within the experimental errors. Especially for Yb^{3+}-doped crystals, when taking the lowest Stark level as the origin of energy and plotting the $^2F_{5/2}$ manifold energy barycenter versus the $^2F_{7/2}$ one, the representative points gen-

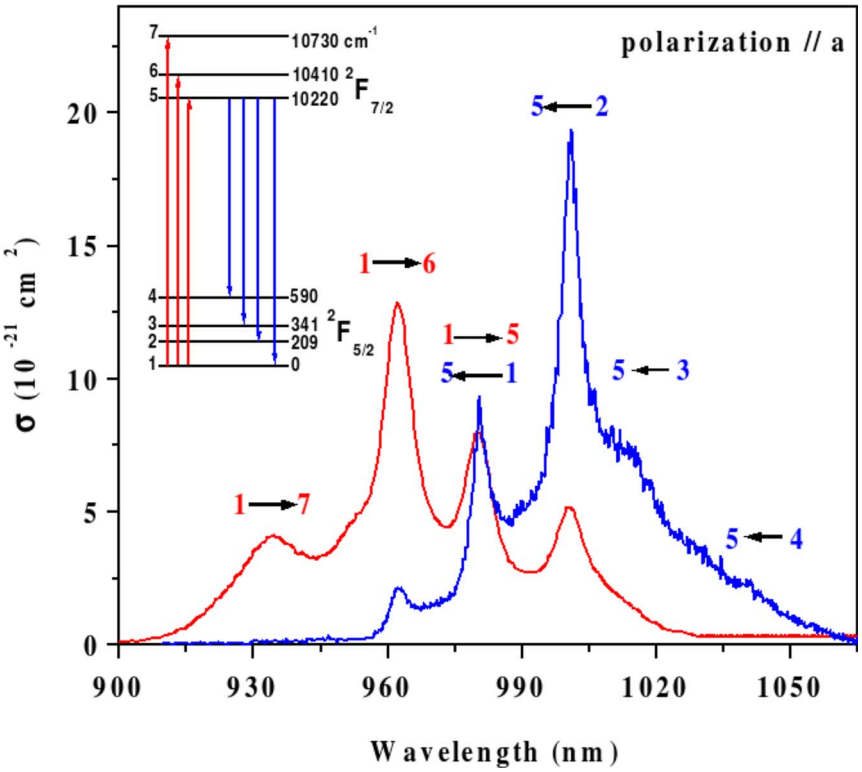

Fig. 5. (Color online) Room-temperature absorption and emission of polarized (// *a* axis) spectra of $Y_{1-x}Yb_xAlO_3$ (with x=0.005).

erally describe a straight line characterized by a slope of unity. In the case of ytterbium, the energy separation between the two manifolds is about 10,200 cm^{-1}. We can neglect the *J* mixing to a good approximation and consider this energy as constant whatever the host. The $^2F_{5/2}$ level barycenter as a function of the $^2F_{7/2}$ level barycenter for several hosts is presented in Fig. 6. According to the assignment of Stark levels of Yb^{3+}:YAP, we have placed values on the barycenter plot to confirm the accuracy of our results, as already discussed, in oxides [1,3,5] and fluorides [7–9]. Stark levels are well positioned on the theoretical slope for this crystal. An important observation can be made: the total splitting of the $^2F_{7/2}$ manifold is smaller (590 cm-1) than the Yb^{3+}-doped YAG one (786 cm-1) that is consequently more favorable for obtaining the population inversion.

C. Concentration-Quenching Analysis

Identifying the origin of the experimental decay concentration dependence allows excited-state dynamics to be understood. Such mechanisms have been studied in oxides and fluorides in our research program and also by different research teams, as it was previously indicated. Figure 7 shows $^2F_{5/2}$ experimental decay time dependence on Yb^{3+} concentration in YAP. We found that decay profiles had exponential behavior to two orders of magnitude at all concentrations. The concentration dependence of Yb^{3+} decay times can be generally divided into two regimes: self-trapping and self-quenching.

1. Self-Trapping Regime

As it can be seen in Fig. 7, the experimental decay time increases up to the maximum at 3.5 mol.%. This is due to the self-trapping or radiative energy transfer between Yb^{3+} neighbor ions via resonant transitions of $^2F_{7/2} \leftrightarrow {}^2F_{5/2}$ stark levels. The resonant transitions are $1\langle-\rangle5$ at any temperature, and $2\langle-\rangle5$ at room temperature. We have to mention a very important feature here: only small volumes of samples were homogeneously excited for all concentrations. Because the volume of materials excited was steady, self-trapping due to a geometrical effect can be supposed to be a constant value for each concentration. The main reason for discrepancies in the literature is that decays were analyzed with big samples showing larger time constants with initial rise times due to strong reabsorption, as we will see below.

Evaluation of the $^2F_{5/2}$ Radiative Lifetime. An evaluation of the radiative lifetime of Yb^{3+}:YAP may also be attempted. Intrinsic lifetimes have received attention for a long time in the literature [25–29]. Measurements of the Yb^{3+} radiative lifetime in crystals require a lot of precaution. As an example, in YAG, measurements of the room-temperature effective stimulated emission cross section have ranged from $1.6\times10^{-20}\,cm^2$ to $2.03\times10^{-20}\,cm^2$

Table 1. Stark Levels of Yb^{3+}:YAP

		Energy (cm^{-1}) $^2F_{7/2}$			Barycenter (cm^{-1})	Energy (cm^{-1}) $^2F_{5/2}$			Barycenter (cm^{-1})
YAP	0	209	341 590	285	10220	10410	10730	10453	

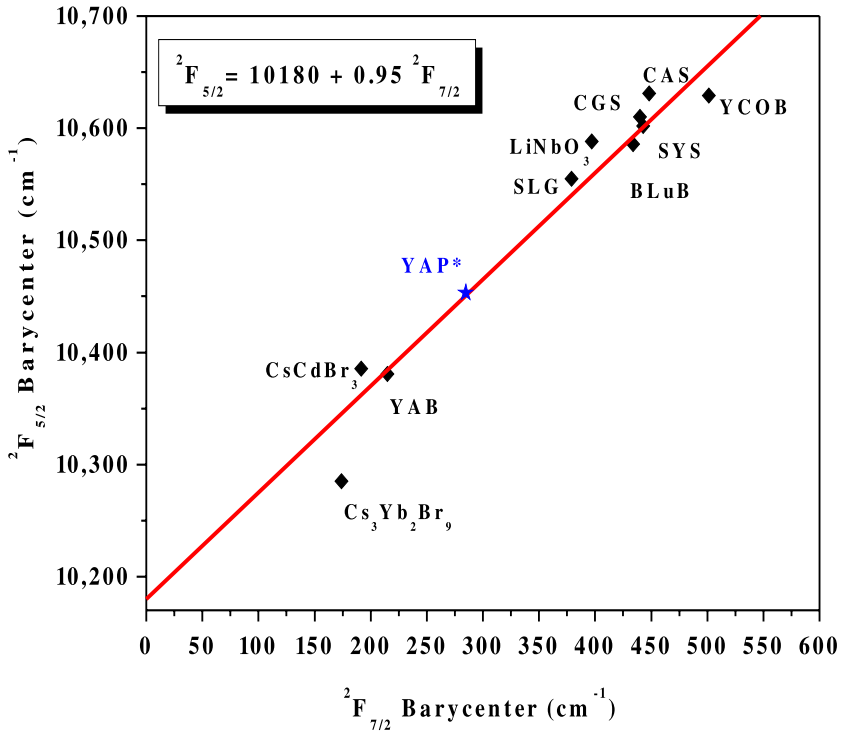

Fig. 6. (Color online) $^2F_{5/2}$ Stark levels barycenter as a function of $^2F_{7/2}$ Stark levels barycenter in different Yb^{3+}-doped hosts.

[1,26]. Depending on the concentration and size of Yb^{3+}-doped samples, we have already observed that the self-trapping process is more or less involved. The intrinsic, or radiative, lifetime can be read by following the concentration dependence to the lowest values in Fig. 7 and has been estimated at 0.60 ms.

The direct calculation of the spontaneous emission probability from the integrated absorption intensity is adapted to confirm the radiative lifetime value. Radiative lifetime can be deduced from the absorption spectrum according to the classical formula:

$$1/\tau_{\text{rad}} = A_{if} = \frac{g_f}{g_i}\frac{8\pi n^2 c}{\lambda_0^4}\int \sigma_{fi}(\lambda)\mathrm{d}\lambda, \qquad (1)$$

where the g's are the degeneracies of the initial and final states (g_f=4 for $^2F_{7/2}$ and g_i=3 for $^2F_{5/2}$), n is the refractive index (n=1.95), c is the light velocity, λ_0 is the mean wavelength of the absorption peak (980 nm), $\sigma(\lambda)$ is the absorption cross section at wavelength λ. The radiative lifetime was calculated as $\tau_{\text{rad(theo.)}}$=0.6 ms by Eq. (1), quite similar to the experimental value of $\tau_{\text{rad(exp.)}}$ =0.6 ms, thus explaining our measurements.

In Yb^{3+}:YAP, the Yb^{3+} radiative lifetimes have not been measured by the combinatorial method, which has been used for YAG [1], Y2O3 [6], CaF2 [7] and KY3F10 [9]. Just to compare, the radiative lifetime has been found at 0.950 ms in Yb^{3+}:YAG—much higher than in Yb^{3+}:YAP. A recent paper [30] has to be mentioned on Yb^{3+}:YAG showing the lifetimes of Yb^{3+} performed as a function of the pinhole size in the annealed YbAG crystal and an Yb(60%):YAG crystal. The intrinsic lifetime is obtained by extrapolating to zero aperture of the pinhole leading to Yb^{3+}-lifetimes of 862±15 and 949±30 μs, respectively, making sense with our data. In Yb^{3+}:YAP all measurements have been done on bulky samples, grown by the CZ technique and taking into account the small excited volume, yielding 0.6 ms for the radiative lifetime.

Discussion and comparison of self-trapping with Yb^{3+}*:*YAG. The difference between Yb^{3+}:YAP and Yb^{3+}:YAG is so surprisingly high. The experimental decay of Yb^{3+}:YAP in Fig. 7 largely increases from 0.60 ms to 0.90 ms below 6 at Yb^{3+}%, whereas the experimental decay of Yb^{3+}:YAG in Fig. 8 increases only slightly by self-trapping from 0.950 ms to 0.988 ms below 6 at Yb^{3+}%. At higher concentrations, decays decrease mainly due to self-quenching [1]. It is clear that self-trapping is much stronger in Yb^{3+}:YAP than in Yb^{3+}:YAG. Consequently self-absorption should be much more efficient in Yb^{3+}:YAP than in Yb^{3+}:YAG. Such conclusion is reached by taking into account the Yb^{3+} concentration difference between the two samples.

Previous results have already been published on 15 at. % Yb^{3+}:YAP and 15 at. % Yb^{3+}:YAG crystals that have been grown using the CZ method [31]. Results indicate that a 15 at. % Yb^{3+}:YAP crystal is a potential candidate for compact, efficient thin-chip lasers when the laser output wavelength is 1012 or 1038 nm through the comparison of the spectroscopic parameters of Yb^{3+}:YAP and Yb^{3+}:YAG. However, concerning decay measurements, there is a large discrepancy between decays published in [31] and results shown in this paper. At 15 at. % Yb^{3+}:YAP for λ_2=1012 nm, a decay of 1.50 ms has been reported, whereas we have measured 0.4 ms using a small volume of the sample. The factor almost equal to 4 between 1.50 ms and 0.4 ms is probably due to an unavoidable strong self-trapping effect in Yb^{3+}:YAP for all the measurements with a greater volume of samples [27]. In

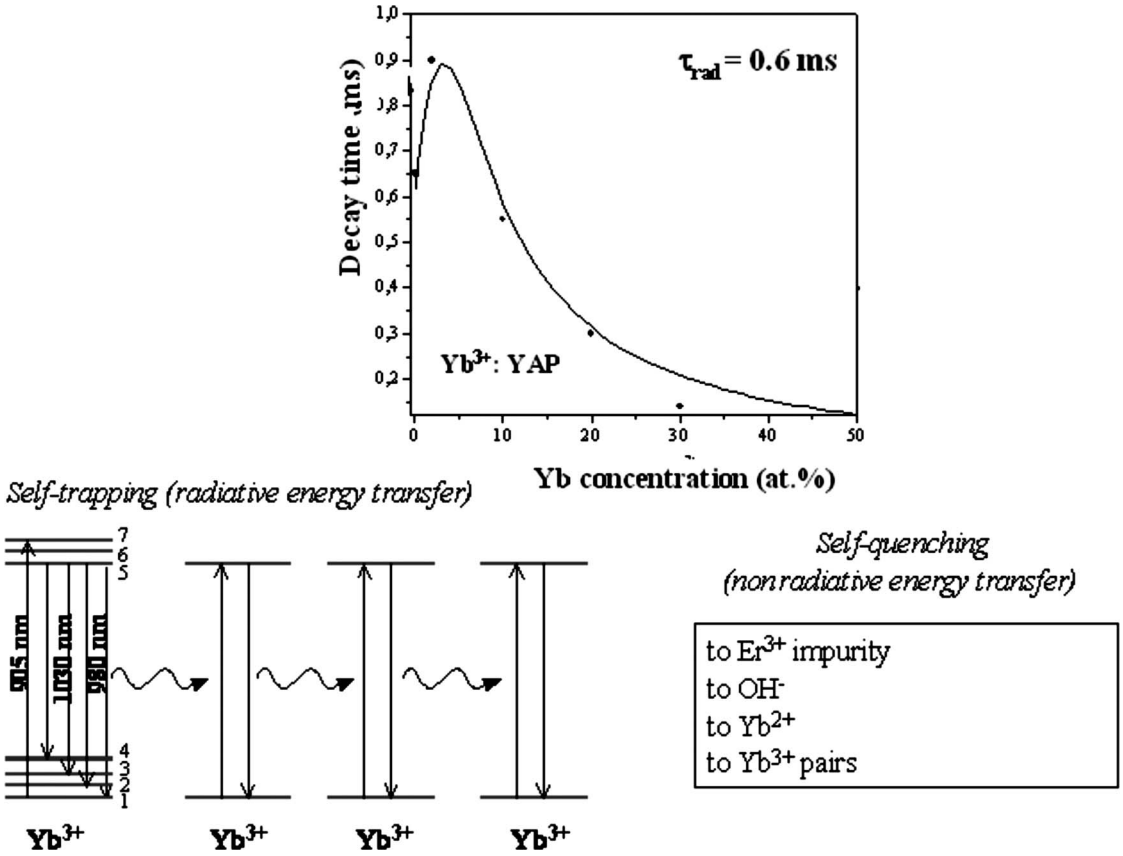

Fig. 7. Concentration dependence of $^2F_{5/2}$ experimental decay time in Yb^{3+}:YAP.

the 15 at. % Yb^{3+}:YAG, the same discrepancy by factor 2 is also observed. That is, less than 0.6 ms in our measurements (see Fig. 8), instead of 1.2 ms as reported at 1029 nm. We think that only measurements of small volumes of matter have physical meaning. This result shows also the limit of the laser spectroscopy technique used to report data.

Wang *et al.* published a recent paper that deals with comparison of fluorescence spectra of Yb^{3+}:YAG and Yb^{3+}:YAP single crystals [32]. The fluorescence spectra of these crystals and the effects of self-absorption on the shape of the fluorescence spectra were studied. All results indicate that the effects of self-absorption on the fluorescence spectra of Yb^{3+}:YAP are remarkably stronger than that of Yb^{3+}:YAG at the same Yb^{3+} concentration. This totally confirms our results described here from decay analysis, which appears as a complementary method of those of the emission spectra concentration dependence. Finally, the comparison of the self-absorption effect from both decays and emission spectrum techniques are consistent.

2. Second Regime: Self-Quenching Process

The second regime, related to the self-quenching effect, corresponds to the higher concentration range of Fig. 7 in which the experimental decay time decreases when the doping rate increases up to 30 mol. %. This is the usual quenching process by energy transfer to defects and other impurities in the host. In the case of Yb^{3+}-doped crystals, because of the presence of only one excited level, we cannot expect an excited-state mechanism as a cross-relaxation process inside Yb^{3+} ions. Research of the main impurities that play the most important role in fluorescence quenching is still very active. Several types of quenching sites, such as other rare-earth impurity ions, OH^- groups, Yb^{3+} pairs, transition metal ions, Yb^{2+}, and color centers in Yb^{3+}-doped crystals, have been reported and will be analyzed.

Evidence of Yb^{3+} *Pairs.* Only pair emission, either from two Yb^{3+} neighbor ions or Yb^{3+} aggregates, also called co-

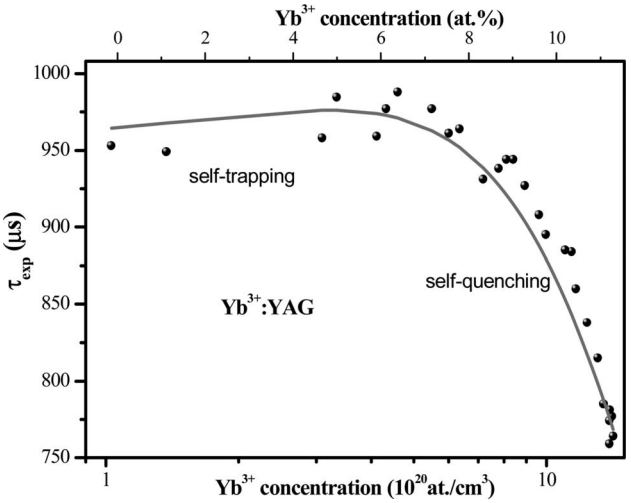

Fig. 8. Concentration dependence of $^2F_{5/2}$ experimental decay time in Yb^{3+}:YAG.

operative emission, can occur in the visible spectrum depending on the shortest distances between Yb^{3+} ions. In Yb^{3+}:YAP crystals, the smallest Yb^{3+}–Yb^{3+} pair distance is 3.6 Å, considering that such a low value is a primary factor for efficient Yb^{3+}–Yb^{3+} pairs.

Figure 9 shows upconversion-visible emission spectra of $Y_{0.80}Yb_{0.20}AlO_3$ crystals under $\lambda = 932$ nm excitation. As can be seen, emission from pairs around 480–510 nm have been effectively detected with time-resolved spectroscopy to avoid strong overlapping of the highest intensity, which is observable at longer time from Er^{3+} and Tm^{3+} rare-earth impurities. The convolution spectrum from the infrared emission spectra has been drawn, as already explained, and we can say that theoretical convolution matches well with the experimental spectra recorded at short time. Consequently, detection of Yb^{3+} pairs is clearly seen in this crystal.

Figure 10 shows the decay curve of $Y_{1-x}Yb_xAlO_3$ (with $x=0.2$) in the spectral range corresponding to a Yb^{3+} pair at around 500 nm. The 500 nm emission exhibits an exponential decay curve characterized by $\tau = 0.20$ ms without any rise time. This value is not exactly half of the $^2F_{5/2}$ decay time ($\tau = 0.30$ ms) as expected for Yb^{3+} pair emissions [33,34]. Higher registered value of the Yb^{3+} pair decay time (0.20 ms instead of 0.15 ms) might be due to an equivalent self-trapping diffusion among pairs, as for the 0-phonon resonant transition, which should increase the decay time.

We would like to add that cooperative luminescence of Yb^{3+}:YAP single crystal has also been recently assigned in the range of 480–520 nm to the cooperative de-excitation of two Yb^{3+} ions but without clear distinction of the difference between pairs' signal and upconversion spectra due to energy transfer between Yb^{3+} and rare-earth impurity ions [35]. In fact, to clearly see pairs, a convolution spectrum of the isolated Yb^{3+} ions emitting in the IR should be compared with time-resolved spectra as was done in Fig. 9. We think that only the remaining upconverted emission bands containing various sharp peaks can be claimed in [35] as the result of $Yb^{3+} \rightarrow Ho^{3+}$, $Yb^{3+} \rightarrow Er^{3+}$ and $Yb^{3+} \rightarrow Tm^{3+}$ energy transfers.

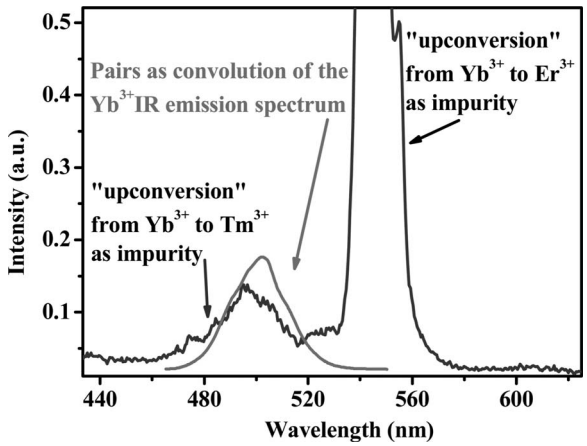

Fig. 9. Time-resolved upconversion visible emission spectrum of $Y_{1-x}Yb_xAlO_3$ (with $x=0.2$) crystals under $\lambda = 932$ nm IR excitation of isolated Yb^{3+} ions. Pairs are clearly detected at short time by convolution of the IR emission spectrum. The Er^{3+} green transition is $^4S_{3/2} \rightarrow {}^4I_{15/2}$. The Tm^{3+} blue transition is $^1G_4 \rightarrow {}^3H_6$.

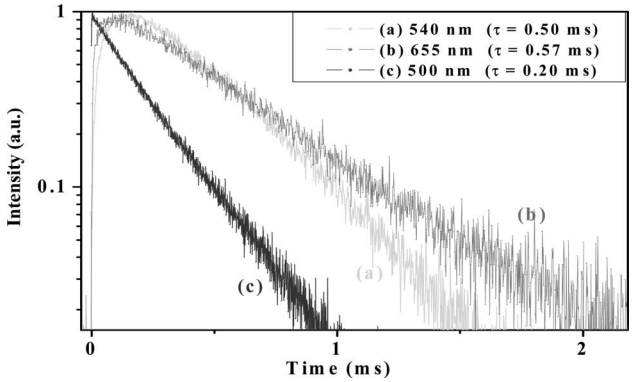

Fig. 10. Decay times of Yb^{3+} pair (500 nm) and Er^{3+} $^4S_{3/2} \rightarrow {}^4I_{15/2}$ (540 nm), $^4F_{9/2} \rightarrow {}^4I_{15/2}$ (655 nm) emissions of $Y_{1-x}Yb_xAlO_3$ (with $x=0.2$).

Unlike in the referenced work, Ho^{3+} impurities have not been detected in this analysis, showing the importance of the initial raw materials on the growth quality of such laser crystals.

Evidence of unwanted rare-earth impurity ions. In samples, the presence of rare-earth impurities was really observed in Fig. 9, even though we started with materials that had a purity of 99.99%. Because rare-earth elements are indeed chemically related, it is difficult to separate them from each other. Thus, impurities are inevitable. The presence of rare-earth impurities was also proven by high-resolution glow discharge mass spectrometry (HR-GDMS), analyzed by Shiva Tec. Europe as the following values in 20% Yb^{3+}:YAP and also in 5% Yb^{3+}:YAG, for comparison (see Table 2).

Moreover, the Dieke diagram in Fig. 11 shows that many resonant energy transfers are possible between trivalent rare-earth ions. In particular, in the 10,000 cm^{-1} energy range, matching with the excited state of Yb^{3+} ions, resonant energy transfer is allowed with the $^4I_{11/2}$ excited level of Er^{3+} ions, and nonresonant energy transfer is also known with the $^3H_5$ excited level of Tm^{3+} ions followed by several upconversion processes. The emission spectrum in Fig. 9 can be assigned as follows:

- The highest intensity between 525 and 575 nm corresponds to the upconversion energy transfer from $^2F_{7/2} \rightarrow {}^2F_{5/2}$ Yb^{3+} absorption transition to $Er^{3+}{}^4I_{11/2} \rightarrow {}^4F_{7/2}$ excited-state absorption followed by the $^4S_{3/2} \rightarrow {}^4I_{15/2}$ green emission [32] and also by $^4F_{9/2} \rightarrow {}^4I_{15/2}$ weak emission at 655 nm.
- The weakest intensity around 480 nm corresponds to Tm^{3+} 3H5 → 3F4 nonradiative relaxation followed by both 3F4 → 3F2 upconversion transition, nonradiative relaxation 3F2 → 3H4, another 3H4 → 1G4 upconversion process, and finally, 1G4 → 3H6 blue emission. Comparison of the intensities means the Tm^{3+} impurity concentration is

Table 2. Impurities in (1) 20% Yb^{3+}:YAP (ppm/wt) and (2) in 5% Yb^{3+}:YAG (ppm/wt)

	Ce	Er	Tm
(1)	0.40	0.16	<0.05
(2)	0.31	0.06	<0.05

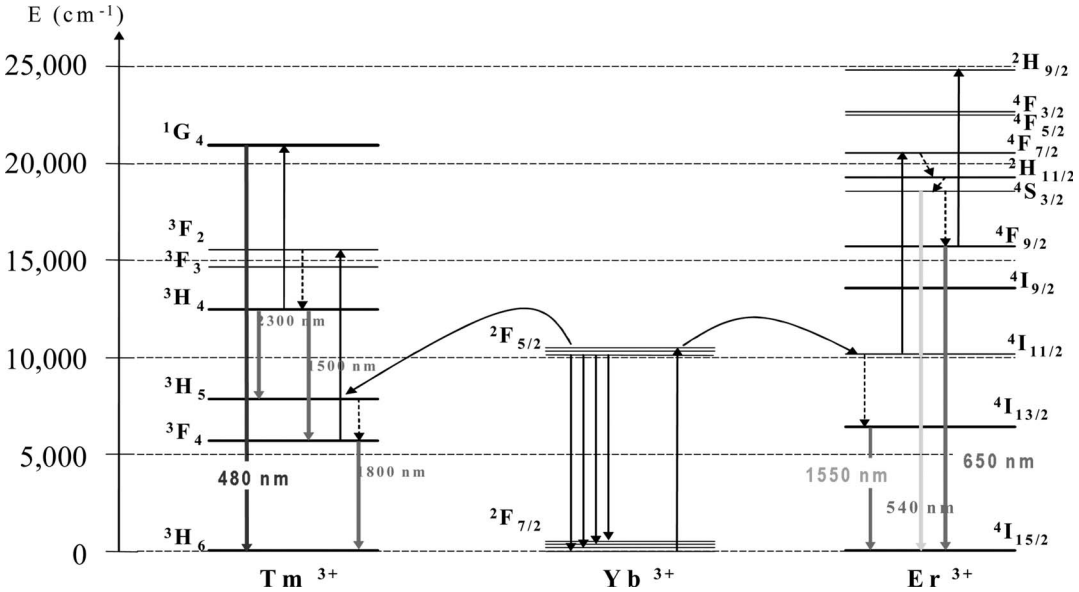

Fig. 11. Energy transfer between Yb^{3+}, Tm^{3+}, and Er^{3+} rare-earth ions according to the Dieke diagram.

weaker in YAP than is that of the Er^{3+} impurity, which explains the analysis in Table 2.

Figure 10 shows decay curve forms of $Y_{1-x}Yb_xAlO_3$ (with $x=0.2$) under Yb^{3+} ion pumping at 932 nm and after energy transfer $Yb^{3+} \rightarrow Er^{3+}$ between two neighbor ions for the corresponding wavelengths of Er^{3+} in the green spectral range $^4S_{3/2} \rightarrow {}^4I_{15/2}$ at 540 nm ($\tau=0.50$ ms for the $^4S_{3/2}$ excited state) and the red spectral range $^4F_{9/2} \rightarrow {}^4I_{15/2}$ at 655 nm ($\tau=0.57$ ms for $^4F_{9/2}$ excited state).

Consequently, decays in the high-dopant-concentration region confirms both the presence of Yb^{3+} pairs, which are characterized by roughly half-decay time of those of $^2F_{5/2}$ Yb^{3+} isolated ions and the energy transfer by upconversion from Yb^{3+} ions to neighbor impurities, leading to deexcitation of mainly, in this case, the Er^{3+} emitting levels according to the model drawn in Fig. 10. As the 540 nm emission from Er^{3+} ions is characterized by an energy transfer, the decay shows an initial rise-time, so that such emission is only observed by time-resolved spectroscopy when we apply a long gate width. Unlike other Yb^{3+}-doped oxides, Tm^{3+} ions were detected only with a very weak intensity in this host, which was confirmed by chemical analysis (<0.05 ppm/wt), then Tm^{3+} decay was not recordable. This result is interesting by itself, since it shows the limit of the laser spectroscopy technique to point out traces of rare-earth impurities.

As a matter of fact, such processes promote a self-quenching phenomenon. This process was observed as concentration quenching in almost all Yb^{3+}-doped oxides we have analyzed [1–9] with probably some little differences caused by the crystal-quality dependence (4N) of each sample. The comparison between 20% Yb^{3+}:YAP and 5% Yb^{3+}:YAG in Table 2 clearly shows higher Er^{3+} impurity concentration in the Yb^{3+} highest concentration. Such difference might also have some weak influence in the lifetime measurements.

Nonradiative energy transfer between Yb^{3+} *and unwanted* OH^- *impurities.* The occurrence of OH^- is very often involved in quenching mechanisms. In oxides OH^- have been shown to exist only as a few traces. There are difficulties in distinguishing the two contributions of both rare-earth ions and OH^- groups in quenching mechanisms. The presence of OH^- groups as traces is proved in the YAP oxide host, as can be seen in Fig. 12. Consequently, it might be another reason for the reduced decays as well as for the strong quenching observed, much stronger than in crystals we have previously studied such as garnets [1–4].

Nonradiative energy transfer between Yb^{3+} *and other types of ions (*Yb^{2+}*, transition metal ions, color centers).* In addition of the impurities analyzed above, several articles mention other centers for quenching mechanisms. We can give mainly two references on this subject [36,30]. As an example, measurements described in [36] on fluorescence lifetimes of Yb:YAG with different doping levels demonstrated that concentration quenching occurs for Yb^{3+} dop-

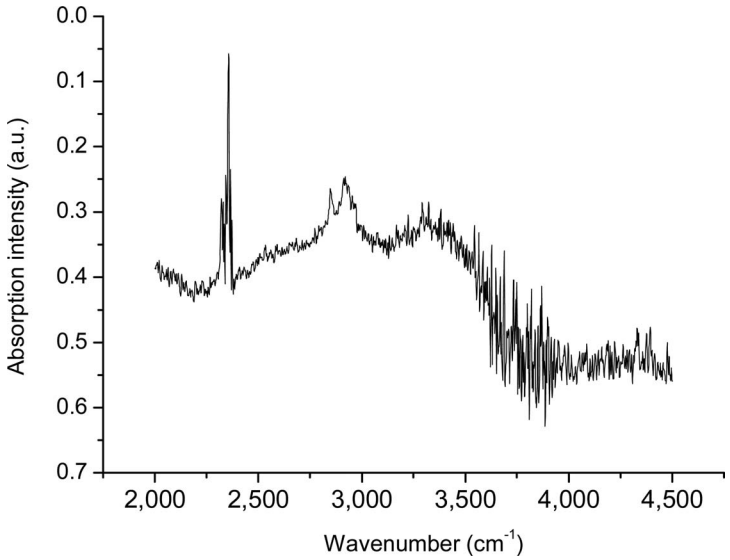

Fig. 12. IR absorption spectrum of OH- impurities in 2 at. % Yb:YAP at around 3300 cm^{-1}.

ing concentration of more than 10 at. %. This phenomenon has been attributed to Yb^{2+}, which results in color center and lattice distortion in the lattice. After annealing at 1600°C in oxygen atmosphere for 24 h, there is $Yb^{2+} \rightarrow Yb^{3+}$ transformation, and both the color center and the lattice distortion were eliminated. Trace impurity ions were detected by means of ICP, which are also responsible for concentration quenching at high-Yb^{3+} doping level.

Another and much more recent paper investigates also the transfer processes in the nonannealed Yb:YAG and YbAG crystals by pointing out the role that might be played by transition metal ions, Yb^{2+}, and color centers [30]. In analogy to the $Yb^{3+} \rightarrow Fe$ transfer, a cooperative energy transfer has been shown between two excited Yb^{3+} ions and one nonexcited Yb^{2+} ion. In addition, nonannealed Yb:YAG and YbAG samples grown from rhenium crucibles indicate that, besides the cooperative quenching of Yb^{2+}, another quenching center should play a role. This second quenching center has been identified as F^+-center charge compensated by a divalent Si ion.

3. Model of Quenching Processes

A model has been submitted to interpret concentration quenching processes and applied to different Yb^{3+}-doped crystals [37]. The self-trapping process has been treated using the approach used for radiation trapping in a gas medium with "weak opacity." It is based on a Compton type spatial diffusion equation containing the Einstein relationships between spontaneous and induced emission and absorption but neglecting the population inversion. In the case of "weak opacity" the previous hypotheses lead to Eq. (2):

$$\tau_t = \tau_i(1 + \sigma N l), \tag{2}$$

where τ_t is the measured lifetime in the trapping conditions, τ_i is the intrinsic lifetime without trapping, σ is the transition cross section, N is the ion doping concentration, and l is the average absorption length in the lifetime measurement experiment.

The theoretical aspects have shown that self-quenching behavior, for a rather large doping range, cannot be explained by fast diffusion toward intrinsic nonradiative centers but is well-described by a limited diffusion process within the doping ion subsystem toward impurities analogous to the doping ions themselves. When the quenching center is an impurity analogous to the active center levels are in resonance or quasi-resonance with the considered ion's first excited state, then the quenching probability can be of the same order as the transfer probability for diffusion within the considered ion subsystem. In such a case, assuming there is an electric dipole–dipole interaction, let's remember that the self-quenching behavior can be simply derived from the following approach.

The self-quenching behavior for the limited diffusion case can be described by a "quenching rate," R_Q, given by Eq. (3) [38]:

$$R_Q = 1/\tau - 1/\tau_w = KN^2, \tag{3}$$

where τ is the measured lifetime at given concentration and τ_w is the measured lifetime at weak concentration; N is the considered active ion concentration. In the general case of nonradiative energy transfer with diffusion within the sensitizers, Weber [39] has explicitly given K in a dipole–dipole hypothesis as

$$K = 8\pi C^{1/4} C_{ss}^{3/4}, \tag{4}$$

where C is the sensitizer-to-activator transfer constant and C_{ss} is the sensitizer-to-sensitizer transfer constant. The general form, for both types of C in Eq. (4), is given by Dexter-type nonradiative transfer theory [38] as

$$C = (R_0/R)^s/\tau_s, \tag{5}$$

where R_0 is a critical transfer distance proportional to the spectral integral overlap assuring the energy conservation during transfer; R is the distance between the two interacting centers; s is the multipolar index ($s=6$ for dipole–dipole), τ_s is the sensitizer lifetime when isolated.

Then we are prompted to look at Eq. (4) under the form $K = 9N_0^2/2\pi\tau_w$ and Eq. (3) becomes

$$\tau(N) = \tau_{rad}/[1 + (9/2\pi)(N/N_0)^2] = \tau_w/[1 + (9/2\pi)(N/N_0)^2], \tag{6}$$

where $\tau_w = \tau_{i=}\tau_{rad}$ is the measured lifetime at weak concentration, which can be adopted as a τ_{rad} radiative lifetime.

We shall consider N_0 as a critical sensitizer concentration for self-quenching. Assuming an homogeneous distribution of sensitizers, it is linked to R_0 by

$$R_0 = (3/4\pi N_0)^{1/3}. \tag{7}$$

Consequently, $\tau(N)$ is indeed the multiplication of the two main processes, as in Eq. (4):

$$\tau(N) = \frac{\tau_{rad}(1 + \sigma N l)}{1 + (9/2\pi)(N/N_0)^2} \tag{8}$$

It is shown that self-quenching of Yb^{3+}:YAP, for a rather large doping range, is well described by a limited diffusion process within at least the doping-ion subsystem toward impurities. The theoretical fittings are shown in Figs. 7 and 8 as a continuous line.

The fitting parameters for Yb^{3+}:YAP were found to be

$$\tau_w = 0.60 \text{ ms}; \quad \sigma l = 1.53 \times 10^{-21} \text{ cm}^3 \ (0.3 \text{ cm}^3/\%);$$

$$\text{and} \quad N_0 = 1.34 \times 10^{21} \text{ cm}^{-3} \ (6.8 \ \%),$$

whereas the fitting parameters for Yb^{3+}:YAG were found to be

$$\tau_w = 0.95 \text{ ms}; \quad \sigma l = 1.9 \times 10^{-22} \text{ cm}^3 \ (0.025 \text{ cm}^3/\%);$$

$$\text{and} \quad N_0 = 2.36 \times 10^{21} \text{ cm}^{-3} \ (17 \ \%) \ [2].$$

Since N_0 is the parameter of self-quenching for crystals of 4N purity, smaller N_0 values than that of Yb^{3+}:YAG mean stronger self-quenching probability.

4. THEORETICAL APPROACH OF LASER MATERIAL OPTIMIZATION

From the results of fittings in Section 3, it is now possible to obtain the experimental points corrected for trapping by a simple deconvolution of the experimental values by

the trapping function (2). The corrected experimental points are shown in Fig. 13(a). On the other hand, by using the fitting parameters, τ_{rad} and N_0, the self-quenching curve simulation as given by Eq. (6) could also be obtained in Fig. 13. As can be seen, the "real" self-quenching curve corresponds to corrected experimental points.

Now, with the help of this continuous reliable mathematical curve for self-quenching, it is possible to determine the material optimum concentration for its active optical use in a simple and unambiguous way [37]. From a steady-state rate equation, the material gain is given by

$$G = \exp[\sigma_g \sigma_a N \tau(N) l], \tag{9}$$

where σ_g is the gain cross section with respect to the quasi-three-level situation for lasers between first excited and ground state, σ_a is the pump absorption cross section for the pumping wavelength, whereas N, $\tau(N)$, and l have been defined above.

From Eq. (9), the product $\tau(N)N$ can be optimized easily. It is plotted in Fig. 13(b) with the axis at right. Since this maximum value is unique, it has been proposed to consider such value in cm^{-3} as an absolute scale for self-quenching characterizing any given host-doping couple. However, concentration of the impurities should also be considered, since it is an essential factor for self-quenching behavior. Here, we noticed once again that the purity of raw materials was 99.99%.

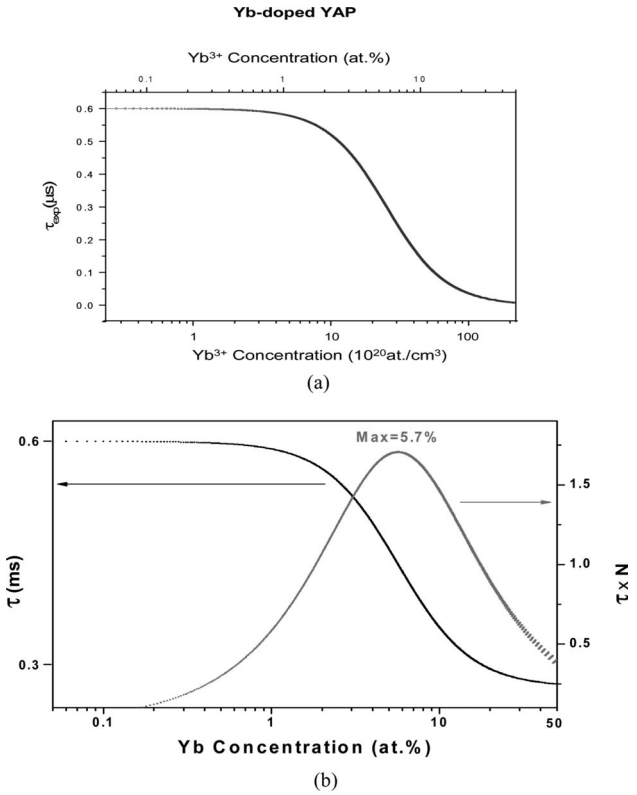

Fig. 13. (a) Concentration dependence of experimental decay times in Yb^{3+}:YAP fitted with correction for the self-trapping effect according to Eq. (6). Two concentration scales have been mentioned both in at. % (upper axis) and 10^{20} at./cm^3 (lower axis). (b) Concentration dependence of experimental decay times in Yb^{3+}:YAP fitted with the theoretical curve for limited-diffusion case according to Eq. (6) compared in the right scale with the optimization of the optical gain by the product $\tau(N)N$. The Yb^{3+} optimum theoretical concentration can be read at the maximum: 5.7 at. %.

As the N_m was found to be equal to $0.83N_0$, the critical concentration itself, which from Eq. (3) can be simply defined as the concentration reducing τ_{rad} to 0.50 τ_{rad}, is a good indication of the self-quenching magnitude and can also easily provide the optimum concentration.

By correcting the self-trapping effect (and considering the maximum of the product $N\tau(N)$, Yb^{3+} optimum concentration is found to be 5.7 at. % in YAP. After correcting the self-trapping effect, the same analysis of the product $N\tau(N)$ in Yb^{3+}:YAG leads to Yb^{3+} optimum concentration of 14.3 at. % not so far from 10% as used in thin laser disks [40,41], which gives some meaning of our own approach. It means that the optimization will be reached at a much lower Yb^{3+} rate in YAP than in YAG, at least by a factor of 3.

Let's mention here results from the Institute for Optical Materials and Technologies of the Belarussian National Technical University on laser properties of $Yb(0.6\%):YAlO_3$, which are published only on the Internet [42]. Efficient continuous-wave diode-pumped lasing was demonstrated for the first time. Output power of 1.2 W at 1040 nm with slope efficiency of 49% was obtained.

5. FIGURE OF MERIT

According to the evaluation of the new figure of merit developed over the past few years [43,44], several Yb^{3+}-doped laser crystals have been compared. This new evaluation is based on a quasi-three-level laser model checked to be close to experimental laser data. The model deals with Gaussian waves, takes into account the saturation of the pump (which occurs for the Yb^{3+} ion because the $^2F_{5/2}$ level has a long lifetime up to 0.9 ms and accumulates population), the stimulated emission at the pump wavelength, the variation of the pump and laser waists along propagation (important for laser-diode pumping), and the variation of the laser intensity along propagation. It is an extension of the model of Risk [45] and Taira [46]. Our evaluation is based on the laser output power and the differential slope extracted from the crystals located inside the same laser cavity and calculated numerically with the model. The pump power has been fixed to 1 W. The laser waist was 22 μm and the pump waist 29 μm. For each crystal we have determined numerically with the model the crystal length L_{opt} and the reflectivity R_{opt} of the output mirror leading to the maximum laser output power.

Calculations from this approach have been applied for both CW oscillator and amplifier regimes and can be visualized in Fig. 14 in a two-dimensional diagram considering the laser extracted power and the slope efficiency. According to this model, which is mainly a comparative one for Yb^{3+}-doped crystals, a first estimation of the spectroscopic potentiality of Yb^{3+}:YAP as a laser material in the IR is less than the Yb^{3+}:YAG one. However, in Yb^{3+}:YAP, the laser beam is naturally polarized, the wavelength at 1010 nm is unusual compared to other oxides such as YAG (1030 nm), the stimulated emission cross-section value is relatively large and, in addition,

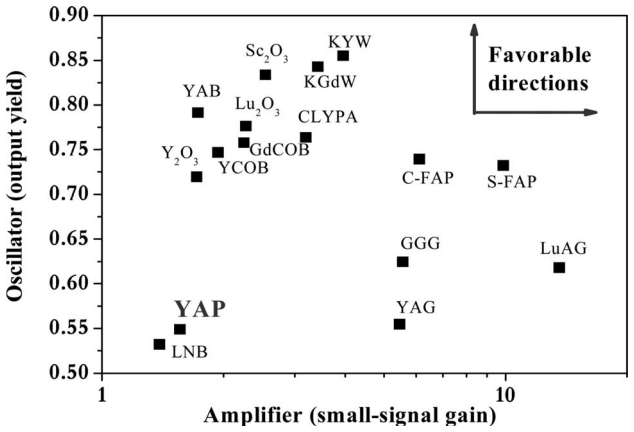

Fig. 14. Figure of merit for several promising Yb^{3+}-doped hosts, including Yb^{3+}:YAP, studied in this work.

undoped-doped-YAP thermal conductivities show comparable values with those of YAG, as we shall demonstrate below, so that a more realistic figure of merit should take into account combined spectroscopic and thermal properties.

6. THERMAL PROPERTIES

As YAP is a biaxial crystal, thermal conductivities have to be measured along *a*, *b*, and *c* axes of the orthorhombic structure. The value corresponding to undoped YAP has been reported as $11\,W\cdot m^{-1}K^{-1}$ [47]. 10% and 30% Yb^{3+}:YAP have been measured recently: 7.2 (*b* axis) and 6.9 (*a* axis) $W\cdot m^{-1}K^{-1}$, respectively, for 10% and 6.3 (*a* axis) and 5.9 (*c* axis), respectively, for 30% [48]. Consequently, high thermal conductivity of Yb^{3+}:YAP can finally improve laser development for polarized laser applications.

7. CONCLUSION

The main objectives of this paper were to describe and analyze the following points about Yb^{3+}-doped YAP: crystal growth, structural characterizations, spectroscopic properties, thermal properties, and figure of merit, based upon the criteria we have previously defined and the gain optimization from the laser model we have previously introduced from concentration-quenching interpretation. A special effort has been made to compare with the properties of Yb^{3+}-doped YAG laser crystal, which is usually taken as reference.

High-optical-quality crystals of Yb^{3+}:YAP perovskite single crystals were grown using the Czochralski method. Samples have been structurally characterized. Yb^{3+} energy levels were assigned and checked by the barycenter law. Experimental decay-time dependence on Yb^{3+} dopant concentrations was studied, suggesting two typical competitive phenomena: the increase of decay time due to strong radiative-energy transfer (self-trapping) and the decrease of decay time due to self-quenching, which is connected to nonradiative-energy transfer from Yb^{3+} ions to impurities, such as both Er^{3+} and Tm^{3+} rare-earth ions, OH- hydroxyl groups, Yb^{3+} pairs analyzed by cooperative luminescence, Yb^{2+} ions with compensator cations and F^+-center charge compensated by a divalent Si ion, as it was recently demonstrated. This general process can be described by a limited diffusion model within the doping ion subsystem to impurities. Let's mention a large discrepancy on decay measurements, already published by previous authors, probably due to strong self-trapping influence related to the large volume of analyzed samples. Important parameters found for laser applications of these samples characterized by 4N purity are Yb^{3+} radiative lifetime, close to 0.60 ms, the self-quenching parameter $N_0 = 1.34\times10^{21}\,cm^{-3}$ (6.8 at. % Yb^{3+}), and the 5.7 at. % Yb^{3+} optimum concentration for laser emission, deduced from a previous model that we proposed a few years ago for Yb^{3+}-doped laser crystals. The position of the figure of merit that we introduced a few years ago confirms the rank of Yb^{3+}:YAP below those of Yb^{3+}-doped garnets.

Consequently, useful spectroscopic basic analyses were found on Yb^{3+}-doped crystals. From the point of view of applications, the main advantages of Yb^{3+}:YAP can be summarized as comparable values of thermal conductivities with those of laser garnets, an unexpected polarized laser wavelength at 1010 nm compared with other oxides such as YAG (1030 nm) and, in addition, large stimulated-emission cross-section values.

ACKNOWLEDGMENTS

The authors acknowledge T. Fukuda at Tohoku University for allowing us the possibility of obtaining samples from J. B. Shim, initially used to study Yb^{3+} charge transfer bands for scintillating applications, and A. Jouini for his assistance in IR absorption measurements. G. B. thanks Luis Humberto da Cunha Andrade GEOF-Grupo de Espectroscopia Óptica e Fototérmica Universidade Estadual de Mato Grosso do Sul-UEMS for discussions.

REFERENCES

1. A. Yoshikawa, G. Boulon, L. Laversenne, H. Canibano, K. Lebbou, A. Collombet, Y. Guyot, and T. Fukuda, "Growth and spectroscopic analysis of Yb3+-doped Y 3 Al 5 O 12 fiber single crystals," J. Appl. Phys. **94**, 5479–5488 (2003).
2. G. Boulon, "Why so deep research on Yb^{3+}-doped optical inorganic materials?" J. Alloys Compd. **451**, 1–11 (2008).
3. Y. Guyot, H. Canibano, C. Goutaudier, A. Novoselov, A. Yoshikawa, T. Fukuda, and G. Boulon, "Yb^{3+}-doped $Gd_3Ga_5O_{12}$ garnet single crystals grown by the micro-pulling-down technique for laser application. Part I: Spectroscopic properties and assignment of energy levels," Opt. Mater. **27**, 1658–1663 (2005).
4. Y. Guyot, H. Canibano, C. Goutaudier, A. Novoselov, A. Yoshikawa, T. Fukuda, and G. Boulon, "Yb^{3+}-doped $Gd_3Ga_5O_{12}$ garnet single crystals grown by the micro-pulling down technique for laser application. Part 2: Concentration quenching analysis and laser optimization," Opt. Mater. **28**, 1–8 (2006).
5. A. Brenier, Y. Guyot, H. Canibano, G. Boulon, A. Ródenas, D. Jaque, A. Eganyan, and A. G. Petrosyan, "Growth

spectroscopic, and laser properties of Yb^{3+}-doped $Lu_3Al_5O_{12}$ garnet crystal," J. Opt. Soc. Am. B **23**, 676–683 (2006).
6. G. Boulon, L. Laversenne, C. Goutaudier, Y. Guyot, and M. T. Cohen-Adad, "Radiative and non-radiative energy transfers in Yb^{3+}-doped sesquioxide and garnet laser crystals from a combinatorial approach based on gradient concentration fibers," J. Lumin. **102**, 417–425 (2003).
7. M. Ito, C. Goutaudier, Y. Guyot, K. Lebbou, T. Fukuda, and G. Boulon, "Crystal growth Yb3+ spectroscopy, concentration quenching analysis and potentiality of laser emission in Ca1-*X*Yb*X*F2+*X*," J. Phys.: Condens. Matter **16**, 1501–1521 (2004).
8. G. Boulon, Y. Guyot, M. Ito, A. Bensalah, C. Goutaudier, G. Panczer, and J. C. Gâcon "From optical spectroscopy to a concentration quenching model and a theoretical approach to laser optimization for Yb^{3+}-doped $YLiF_4$ crystals," Mol. Phys. **102**, 1119–1132 (2004).
9. M. Ito, G. Boulon, A. Bensalah, Y. Guyot, C. Goutaudier, and H. Sato "Spectroscopic properties, concentration quenching, and prediction of infrared laser emission of Yb^{3+}-doped KY_3F_{10} cubic crystal," J. Opt. Soc. Am. B **24**, 3023–3033 (2007).
10. G. A. Massey, "Measurement of devices parameters for Nd:YAlO3 lasers,"I IEEE J. Quantum Electron. **8**, 669–674 (1972).
11. M. J. Weber, "Optical spectra of Ce^{3+} and Ce^{3+}-sensitized fluorescence in $YAlO_3$," J. Appl. Phys. **44**, 3205–3208 (1973).
12. T. Takeda, T. Miyata, F. Muramatsu, and T. Tomiki, "Fast decay U.V. Phosphor-$YAlO_3$:Ce," J. Electrochem. Soc. **127**, 438–444 (1980).
13. M. Nikl, "Wide band gap scintillation materials: progress in the technology and material understanding," Phys. Status Solidi A **178**, 595–601 (2000).
14. S. Belogurov, G. Bressi, G. Carugno, M. Moszynski, W. Czarnacki, M. Kapusta, and M. Szawlowski, "Characterization of Yb:YAG and Yb:YAP scintillators by means of LAAPD at temperature around 100 K," Nucl. Instrum. Methods Phys. Res. A **496**, 385–404 (2003).
15. R. Ifflander, *Solid-State Lasers for Materials Processing, Fundamental Relations and Technical Realizations* (Springer-Verlag, 2001).
16. M. J. Weber, M. Bass, and K. Andringa, "Czochralski growth and properties of $YAlO_3$ laser crystals," Appl. Phys. Lett. **15**, 342–345 (1969).
17. I. A. Kamenskikh, N. Guerassimova, C. Dujardin, N. Garnier, G. Ledoux, C. Pedrini, M. Kirm, A. Petrosyan, and D. Spassky, "Charge transfer fluorescence and f–f luminescence in ytterbium compounds," Opt. Mater. **24**, 267–274 (2003).
18. I. A. Kamenskikh, C. Dujardin, N. Garnier, N. Guerassimova, G. Ledoux, V. Mikhailin, C. Pedrini, A. Petrosyan, and A. Vasil'ev, "Temperature dependence of the charge transfer and f-f luminescence of Yb^{3+} in garnets and YAP," J. Phys.: Condens. Matter **17**, 5587–5594 (2005).
19. A. Yoshikawa, H. Ogino, J. B. Shim, M. Nikl, N. Solovieva, and T. Fukuda, "Growth and luminescent properties of Yb^{3+}-doped oxide single crystals for scintillator application," Radiat. Meas. **38**, 467–470 (2004).
20. J. B. Shim, A. Yoshikawa, M. Nikl, N. Solovieva, J. Pejchal, D. H. Yoon, and T. Fukuda, "Growth and characterization of Yb^{3+}-doped $YAlO_3$ fiber single crystals grown by the modified micro-pulling-down method," J. Cryst. Growth **256**, 298–304 (2003).
21. J. B. Shim, A. Yoshikawa, T. Fukuda, J. Pejchal, M. Nikl, N. Sarukura, and D. H. Yoon, "Growth and charge transfer luminescence of Yb^{3+}-doped $YAlO_3$ single crystals," J. Appl. Phys. **95**, 3063–3068 (2004).
22. A. Yoshikawa, H. Ogino, J. B. Shim, V. V. Kochurikin, M. Nikl, N. Solovieva, S. Ono, N. Sarukura, M. Kikuchi, and T. Fukuda, "Growth and scintillation properties of Yb doped aluminate, vanadate and silicate single crystals," Opt. Mater. **26**, 529–534 (2004).
23. L. D. DeLoach, S. A. Payne, L. L. Chase, L. K. Smith, W. L. Kway, and W. F. Krupke, "Evaluation of absorption and emission properties of Yb[3+] doped crystals for laser applications," IEEE J. Quantum Electron. **29**, 1179–1191 (1993).
24. P.-H. Haumesser, R. Gaume, B. Viana, E. Antic-Fidancev, and D. Vivien, "Spectroscopic and crystal field analysis of new Yb-doped laser materials," J. Phys.: Condens. Matter **13**, 5427–5447 (2001).
25. D. S. Sumida and T. Y. Fan, "Effect of radiation trapping on fluorescence lifetime and emission cross section measurements in solid-state laser media," Opt. Lett. **19**, 1343–1345 (1994).
26. N. Uehara, K. Ueda, and Y. Kubota, "Spectroscopic measurement of a high-concentration Yb^{3+}:LiYF 4 crystal," Jpn. J. Appl. Phys., Part 1 **35**, L499–L501 (1996).
27. M. P. Hehlen, "Effect of radiation trapping on measured excited-state lifetimes in solids," in *OSA TOPS on Advanced Solid-State Lasers*, S. A. Payne and C. Pollock, Eds., Vol. 1 (Optical Society of America, 2006) p. 530.
28. H. P. Christensen, D. R. Gabbe, and H. P. Jenssen, "Fluorescence lifetimes for neodymium-doped yttrium aluminum garnet and yttrium oxide powders," Phys. Rev. B **25**, 1467–1473 (1982).
29. H. W. Bruesselbach, D. S. Sumida, R. A. Reeder, and R. W. Byren, "Low-heat high-power scaling using InGaAs-diode-pumped Yb:YAG lasers," IEEE J. Sel. Top. Quantum Electron. **3**, 105–116 (1997).
30. D. Fagundes-Peters, N. Martynyuk, K. Lünstedt, V. Peters, K. Petermann, G. Huber, S. Basun, V. Laguta, and A. Hofstaetter, "High quantum efficiency YbAG-crystals," J. Lumin. **125**, 238–247 (2007).
31. X. Zeng, G. Zhao, X. Xu, H. Li, J. Xu, Z. Zhao, X. He, H. Pang, M. Y. Jie, and C. Yan, "Comparison of spectroscopic parameters of 15 at % Yb:$YAlO_3$ and 15 at % Yb:$Y_3Al_5O_{12}$," J. Cryst. Growth **274**, 106–112 (2005).
32. X. Wang, X. Xu, Z. Zhao, B. Jiang, J. Xu, G. Zhao, P. Deng, G. Bourdet, and J.-C. Chanteloup, "Comparison of fluorescence spectra of Yb:$Y_3Al_5O_{12}$ and Yb:$YAlO_3$ single crystals," Opt. Mater. **29**, 1662–1666 (2007).
33. E. Nakazawa and S. Shionoya, "Cooperative luminescence in $YbPO_4$," Phys. Rev. Lett. **25**, 1710–1712 (1970).
34. Y. Guyot, R. Moncorgé, L. D. Merkle, A. Pinto, B. McIntosh, and H. Verdun, "Luminescence properties of Y_2O_3 single crystals doped with Pr^{3+} or Tm^{3+} and codoped with Yb^{3+}, Tb^{3+} or Ho^{3+} ions," Opt. Mater. **5**, 127–136 (1996).
35. Y. Dong, G. Zhou, J. Xu, G. Zhao, F. Su, L. Su, G. Zhang, D. Zhang, H. Li, and J. L. Si, "Cooperative and charge transfer luminescence in Yb^{3+}-doped yttrium aluminum perovskite (YAlO3)," J. Cryst. Growth **289**, 676–680 (2006).
36. P. Yang, P. Deng, and Z. Yin, "Concentration quenching in Yb:YAG," J. Lumin. **97**, 51–54 (2002).
37. F. Auzel, G. Baldacchini, L. Laversenne, and G. Boulon, "Radiation trapping and self-quenching analysis in Yb3+, Er3+, and Ho3+ doped Y2O3," Opt. Mater. **24**, 103–109 (2003).
38. F. Auzel, "Materials for ionic solid state lasers," in *Spectroscopy of Solid-State Laser-Type Materials*, B. DiBartolo, ed. (Plenum, 1987), p. 293.
39. M. J. Weber, "Luminescence decay by energy migration and transfer: observation of diffusion-limited relaxation," Phys. Rev. B **4**, 2932–2939 (1971).
40. T. Taira and M. Tsunekane, "High-power edge pumped Yb:YAG single crystal/YAG ceramics hybrid microchip laser," Proc. SPIE **6216**, 621607 (2006).
41. M. Tsunekane and T. Taira, "High-power operation of diode edge-pumped, glue-bonded, composite Yb:Y3Al5O12 microchip laser with ceramic, undoped YAG pump light-guide," Jpn. J. Appl. Phys., Part 2 **44**, L 1164–L 1167 (2005).
42. Kuleshov, from Minsk at the ICONO/LAT 2007 http://www1.ilc.by/news/news-002.html (May 2007).
43. A. Brenier and G. Boulon, "Overview of the best Yb^{3+}-doped laser crystals," J. Alloys Compd. **323-324**, 210–213 (2002).

44. A. Brenier and G. Boulon, "New criteria to choose the best Yb^{3+}-doped laser crystals," Europhys. Lett. **55**, 647–652 (2001).
45. W. P. Risk, "Modeling of longitudinally pumped solid-state lasers exhibiting reabsorption losses," J. Opt. Soc. Am. B **5**, 1412–1423 (1988).
46. T. Taira, W. M. Tulloch, and R. L. Byer, "Modeling of quasi-three-level lasers and operation of CW Yb:YAG lasers," Appl. Opt. **36**, 1867–1874 (1997).
47. S. S. Ballard and J. S. Browle, *Handbook of Laser Science and Technology, Vol. IV, Optical Materials, Part 2* (CRC Press, 1986), p. 49.
48. J. Petit, "Monocristaux dopés ytterbium et matériaux assemblés pour lasers de fortes puissances," Ph.D. dissertation (Université Pierre and Marie Curie-Paris VI, 2006).